Inhibition of impulsive action by projection-defined prefrontal pyramidal neurons

Bing Li[a,b], Thao Phuong Nguyen[c,1], Chenyan Ma[a,b], and Yang Dan[a,b,2]

[a]Division of Neurobiology, Department of Molecular and Cell Biology, Helen Wills Neuroscience Institute, University of California, Berkeley, CA 94720; [b]Howard Hughes Medical Institute, University of California, Berkeley, CA 94720; and [c]Bioengineering and Materials Science Engineering, University of California, Berkeley, CA 94720

Contributed by Yang Dan, May 7, 2020 (sent for review January 10, 2020; reviewed by Carlos D. Brody and Garret D. Stuber)

The prefrontal cortex (PFC) plays a critical role in curbing impulsive behavior, but the underlying circuit mechanism remains incompletely understood. Here we show that a subset of dorsomedial PFC (dmPFC) layer 5 pyramidal neurons, which project to the subthalamic nucleus (STN) of the basal ganglia, play a key role in inhibiting impulsive responses in a go/no-go task. Projection-specific labeling and calcium imaging showed that the great majority of STN-projecting neurons were preferentially active in no-go trials when the mouse successfully withheld licking responses, but lateral hypothalamus (LH)-projecting neurons were more active in go trials with licking; visual cortex (V1)-projecting neurons showed only weak task-related activity. Optogenetic activation and inactivation of STN-projecting neurons reduced and increased inappropriate licking, respectively, partly through their direct innervation of the STN, but manipulating LH-projecting neurons had the opposite effects. These results identify a projection-defined subtype of PFC pyramidal neurons as key mediators of impulse control.

prefrontal cortex | impulsive behavior | subthalamic nucleus | lateral hypothalamus | two-photon calcium imaging

Impulse control is an essential cognitive process that allows the animal to inhibit inappropriate habitual responses and facilitate behaviors consistent with the internal goal (1–3). A simple behavioral paradigm well suited for measuring response inhibition is the go/no-go task, in which the subject is required to respond to the go stimulus but withhold response to the no-go stimulus. Previous studies in multiple species have shown that lesions in the prefrontal cortex (PFC) cause marked increases in false-alarm errors (inappropriate responses in no-go trials) (e.g., refs. 4 and 5), and optogenetic inactivation of the mouse dorsomedial PFC (dmPFC) demonstrated the importance of its activity on a trial-by-trial basis (6). In tasks that require waiting for a sensory cue before making a motor response, lesion or inactivation of the rat dmPFC also increased premature response errors (7–10). Together, these findings indicate a critical role of the rodent dmPFC in inhibiting impulsive responses.

A variety of task-related signals have been observed in PFC neuron activity, including those associated with sensory cues, motor actions, and task outcomes (reward and punishment) (9, 11–14). Within a given PFC subregion, different subtypes of inhibitory interneurons—labeled by distinct molecular markers—are preferentially activated by different task-related events, but neurons of the same subtype exhibit similar activity (15). PFC pyramidal neurons also exhibit a high degree of functional heterogeneity, but its relationship with molecularly defined cell types is much less understood. During a delayed go/no-go task, the delay-period activity of some pyramidal neurons in mouse dmPFC is higher in no-go trials (NG-preferring), signaling the intention to withhold the motor response, but other neurons are selectively active in go trials (go-preferring) (6), similar to that found in the motor cortex (16). Although the NG-preferring neurons are outnumbered by go-preferring neurons, nonselective inhibition of pyramidal neuron activity caused much more false alarms (FAs) than misses (failure to respond in go trials), suggesting that the NG-preferring neurons are crucial for response inhibition. Calcium imaging showed that NG-preferring neurons are more abundant in deep than superficial cortical layers, but even in deep layers, there are many go-preferring neurons intermingled with NG-preferring neurons (6). This makes it difficult to target the NG-preferring neurons selectively to examine the cause and consequence of their activation in go/no-go behavior.

Previous studies in sensory (17–20), motor (21, 22), and prefrontal (23–25) cortical areas have shown that the functional properties of neurons are correlated with their projection targets. For response inhibition, a growing number of studies have indicated the importance of the subthalamic nucleus (STN) in the basal ganglia (26–33), which receives direct input from the PFC through the hyperdirect pathway (34). This raises the possibility that response inhibition in no-go trials is partly mediated by STN-projecting dmPFC neurons. To test this hypothesis, we selectively labeled the dmPFC pyramidal neurons projecting to the STN, visual cortex (V1), or lateral hypothalamus (LH) using a retrograde virus. Calcium imaging showed that the great majority of STN-projecting neurons are NG-preferring, whereas most of the LH-projecting neurons are go-preferring; V1-projecting neurons showed only weak go or no-go preference. Optogenetic activation of STN-projecting dmPFC neurons or their axons in the STN markedly improved task performance mainly by reducing the FA rate, whereas inactivating these neurons had the opposite effect. In contrast, bidirectional

Significance

The prefrontal cortex (PFC) has long been recognized as a crucial region for suppressing impulsive behavior, but the specific neurons mediating the effect remained elusive. Using projection-specific labeling of PFC neurons for imaging and optogenetic manipulation in mice performing a go/no-go task, we showed that the subset of layer 5 pyramidal neurons projecting to the subthalamic nucleus, but not those projecting to the lateral hypothalamus or visual cortex, play a critical role in inhibiting impulsive responses. Our demonstration of a distinct functional property of a projection-defined PFC pyramidal neuron population provides an important entry point for delineating the PFC circuit underlying impulse control.

Author contributions: B.L. and Y.D. designed research; B.L. and T.P.N. performed research; C.M. contributed new reagents/analytic tools; B.L. analyzed data; and B.L. and Y.D. wrote the paper.

Reviewers: C.D.B., Princeton University; and G.D.S., University of Washington.

The authors declare no competing interest.

Published under the PNAS license.

[1]Present address: Department of Biomedical Engineering, Northwestern University, Evanston, IL 60208.

[2]To whom correspondence may be addressed. Email: ydan@berkeley.edu.

This article contains supporting information online at https://www.pnas.org/lookup/suppl/doi:10.1073/pnas.2000523117/-/DCSupplemental.

First published July 6, 2020.

Downloaded at Palestinian Territory, occupied on December 11, 2021

www.manaraa.com

manipulation of LH-projecting neurons showed that their activity impairs performance by increasing the FA rate. Together, these results show that STN-projecting dmPFC pyramidal neurons play a critical role in impulse control through the hyperdirect pathway.

Results

Different dmPFC Layer 5 Neurons Project to STN, V1, and LH. The projection from the PFC to the STN originates primarily from pyramidal tract neurons in layer 5 (35, 36). To compare the STN-projecting and other neuronal populations in the same layer, we used *Rbp4*^{Cre} mice, which express Cre-recombinase specifically in layer 5 pyramidal neurons (37). Injection of Cre-inducible adeno-associated virus expressing mCherry (AAV2-EF1α-DIO-mCherry) into the dmPFC of *Rbp4*^{Cre} mice revealed multiple projection targets. In addition to the ipsilateral STN, layer 5 neurons also project bilaterally to the LH and V1 among other brain areas (Fig. 1 *A* and *B* and *SI Appendix*, Fig. S1).

We then performed dual retrograde labeling to identify dmPFC neurons that are separate from those projecting to the STN (referred to as "PFC$^{\rightarrow STN}$ neurons"). Previous studies showed that PFC$^{\rightarrow STN}$ neurons send axon collaterals to multiple brain regions but not sensory cortices such as V1 (35). Indeed, Cre-inducible retrograde AAVs (38) expressing mCherry (rAAV2-retro-EF1α-DIO-mCherry) and eGFP (rAAV2-retro-EF1α-DIO-eGFP) injected into the STN and V1, respectively, labeled distinct layer 5 populations (Fig. 1 *C–E*), although the incomplete retrograde labeling of each population is likely to result in underestimation of the overlap (*Discussion*). The different spatial distributions of mCherry- and eGFP-labeled neurons (Fig. 1 *F* and *G*) ($P = 7.7 \times 10^{-6}$, Kolmogorov–Smirnov test) are consistent with the notion that PFC$^{\rightarrow V1}$ neurons are intratelencephalic, separate from PFC$^{\rightarrow STN}$ pyramidal tract neurons (36, 39). Another major projection target of the dmPFC is the LH (Fig. 1*B*), in which GABAergic neurons strongly promote reward-seeking behaviors (40). Dual retrograde tracing showed that PFC$^{\rightarrow LH}$ layer 5 neurons are largely distinct from both PFC$^{\rightarrow V1}$ and PFC$^{\rightarrow STN}$ populations (Fig. 1 *C–H*). We thus compared the functional roles of these three dmPFC layer 5 populations in response inhibition.

Activity of PFC$^{\rightarrow STN}$, PFC$^{\rightarrow V1}$, and PFC$^{\rightarrow LH}$ Neurons during Go/No-Go Task. We trained head-fixed mice on a delayed go/no-go task (Fig. 2 *A* and *B*). During each trial, either a go (17 kHz) or no-go (9 kHz) auditory cue was presented, and the response period began when a water port was presented. Licking in go trials within the response window (hit) was rewarded, but licking in no-go trials (FA) was punished; licking outside of the response window was ignored. A 2-s delay period was inserted between the cue and response periods, allowing us to examine the temporal dynamics of dmPFC activity separate from the cue-evoked and reward/punishment-evoked responses. Mice learned this task within several weeks, licking mostly during the response window (*SI Appendix*, Fig. S2*A*) and performing at ∼80% correct rate (*SI Appendix*, Fig. S2*B*). Similar to previous studies (6, 15), most of the errors were FAs rather than misses, indicating that the performance depends mainly on successful inhibition of inappropriate responses.

To measure the activity of each layer 5 neuronal population, we injected Cre-inducible rAAV2-retro expressing GCaMP6s (38, 41) into the STN, V1, or LH of *Rbp4*^{Cre} mice (Fig. 2*A*).

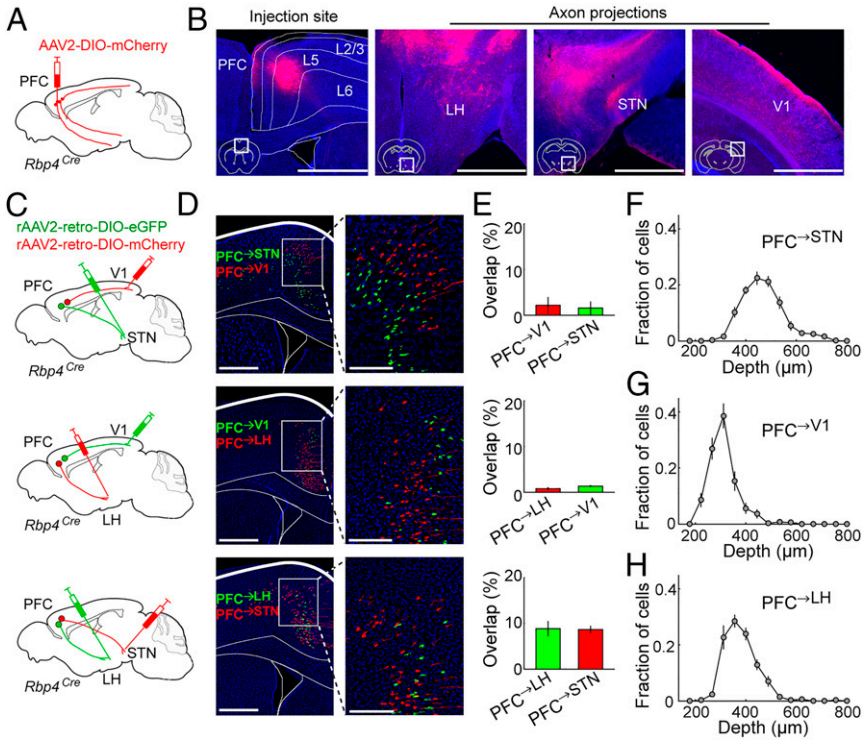

Fig. 1. Different dmPFC layer 5 neurons project to STN, V1, and LH. (*A*) Virus injection for tracing axonal projections from dmPFC layer 5 neurons. (*B*) Fluorescence images of the injection site (white box in coronal diagram) and several ipsilateral projection targets. Red, mCherry; blue, 4′,6-diamidino-2-phenylindole dihydrochloride (DAPI). (Scale bar, 1 mm.) (*C*) Injection procedure for dual retrograde tracing. (*D*) Fluorescence images of retrogradely labeled PFC neurons. (*Right*) Enlarged view of the region in white box (*Left*). Red, mCherry; green, eGFP; blue, DAPI. (Scale bar, *Left*, 500 μm, and *Right*, 100 μm.) (*E*) Quantification of overlap between each pair of projection-defined populations ($n = 3$ mice each). Spatial distribution of (*F*) PFC$^{\rightarrow STN}$ ($n = 6$ mice), (*G*) PFC$^{\rightarrow V1}$ ($n = 6$ mice), and (*H*) PFC$^{\rightarrow LH}$ ($n = 6$ mice) neurons. The three distributions are significantly different (PFC$^{\rightarrow STN}$ vs. PFC$^{\rightarrow V1}$, $P = 7.7 \times 10^{-6}$; PFC$^{\rightarrow LH}$ vs. PFC$^{\rightarrow V1}$, $P = 0.03$; PFC$^{\rightarrow STN}$ vs. PFC$^{\rightarrow LH}$, $P = 0.006$; Kolmogorov–Smirnov test, Bonferroni–Holm corrected). All error bars indicate ±SEM.

Downloaded at Palestinian Territory, occupied on December 11, 2021

www.manaraa.com

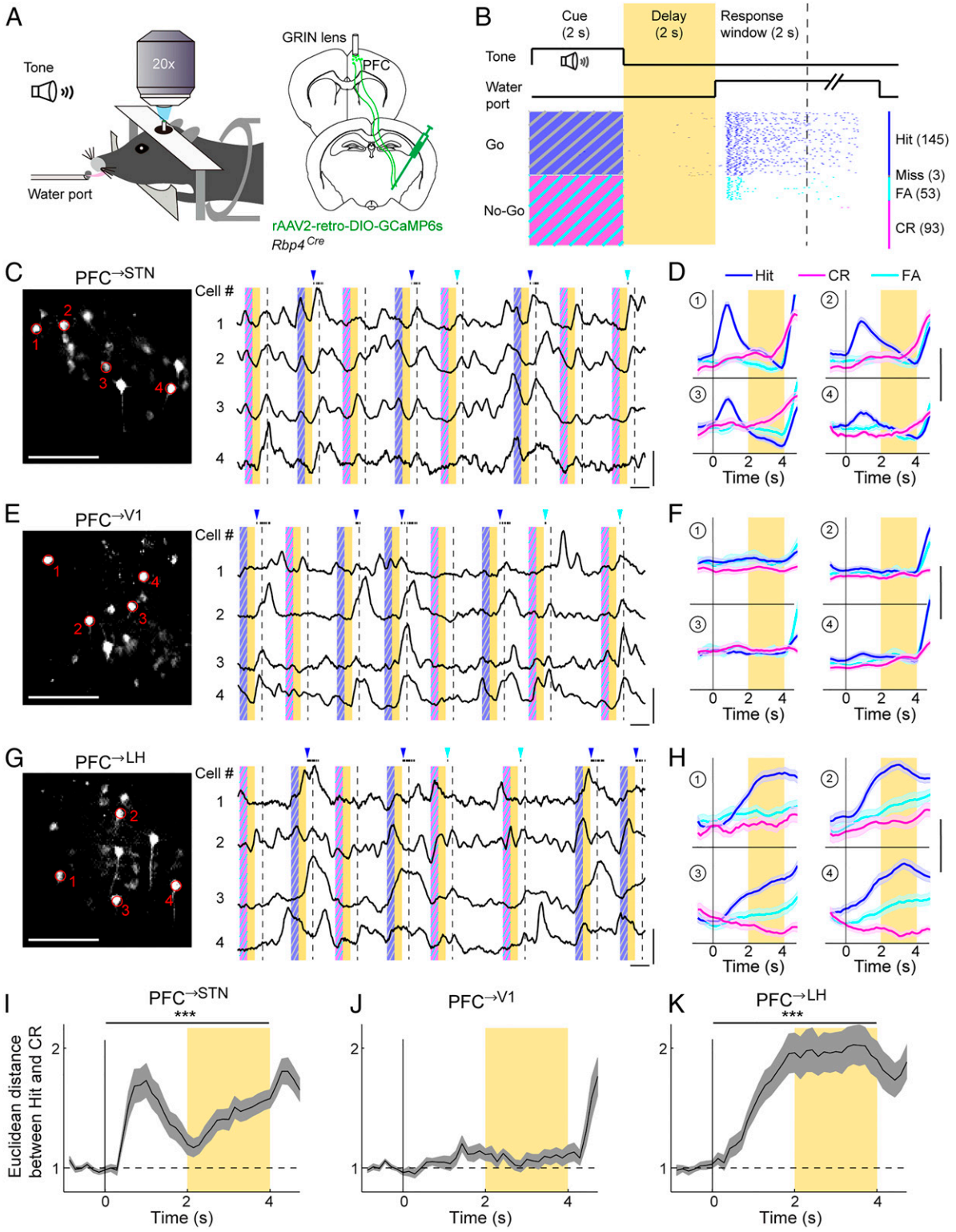

Fig. 2. Activity of PFC$^{\rightarrow STN}$, PFC$^{\rightarrow V1}$, and PFC$^{\rightarrow LH}$ neurons during go/no-go task. (*A*) Schematic of calcium imaging during task. (*B*) Schematic for the task structure (*Top*) and an example behavioral session (*Bottom*). Each tick indicates one lick. Yellow shading indicates delay period. Dashed line indicates end of response window. Numbers in brackets indicate the number of trials of each type. (*C*) (*Left*) Field of view in an example imaging session for PFC$^{\rightarrow STN}$ neurons. Red outlines indicate example cells shown on the right. (Scale bar, 100 μm.) (*C*) (*Right*) Raw fluorescence traces of the example ROIs. Yellow shading indicates delay period; blue/magenta stripes indicate cue periods with target/nontarget tones, respectively. Dashed line indicates end of response window. Black ticks on top are lick responses. Blue/cyan arrowheads indicate delivery of reward/punishment. (Vertical scale bar, 3 Z scores; horizontal scale bar, 5 s.) (*D*) Trial-averaged activity of the example ROIs. Shading indicates ±SEM. (Scale bar, 1 Z score.) (*E* and *F*) Similar to *C* and *D* but for PFC$^{\rightarrow V1}$ neurons. (*G* and *H*) Similar to *C* and *D* but for PFC$^{\rightarrow LH}$ neurons. (*I*) Euclidean distance between the population activity in the correct go (hit) and no-go (CR) trials for PFC$^{\rightarrow STN}$ neurons. The distance during the cue and delay periods was significantly higher than baseline ($P = 1.9 \times 10^{-7}$, Wilcoxon rank sum test, $n = 6$ mice, ***$P < 0.001$). (*J*) Similar to *I* but for PFC$^{\rightarrow V1}$ neurons ($P = 0.69$, $n = 6$ mice). (*K*) Similar to *I* but for PFC$^{\rightarrow LH}$ neurons ($P = 1.2 \times 10^{-5}$, $n = 6$ mice).

Downloaded at Palestinian Territory, occupied on December 11, 2021
www.manaraa.com

Two-photon calcium imaging was performed in the dmPFC through a gradient refractive index (GRIN) lens. All three retrogradely labeled populations exhibited robust activity during the response window (Fig. 2 *C*, *E*, and *G*), largely reflecting widespread responses to reward and punishment (15). To understand the circuit mechanism for response inhibition, we focused on activity before the response window for the remainder of the study. During the cue and delay periods, the percentage of neurons with task-modulated activity ($P < 0.01$, two-way ANOVA; *Materials and Methods*) was significantly higher among PFC$^{\rightarrow STN}$ (79.8%) and PFC$^{\rightarrow LH}$ (69.1%) than PFC$^{\rightarrow V1}$ (54.4%) neurons ($P = 5.7 \times 10^{-4}$, χ^2 test). Whereas large fractions of PFC$^{\rightarrow STN}$ and PFC$^{\rightarrow LH}$ neurons showed different activity in go and no-go trials, most PFC$^{\rightarrow V1}$ neurons were indifferent to the trial type (Fig. 2 *D*, *F*, and *H*), as quantified by the Euclidean distance between the population activity in the correct go (hit) and no-go (CR) trials (Fig. 2 *I*–*K*).

Go vs. No-Go Preference of PFC$^{\rightarrow STN}$ and PFC$^{\rightarrow LH}$ Neurons. Although both PFC$^{\rightarrow STN}$ and PFC$^{\rightarrow LH}$ neurons encode the upcoming motor response, they exhibit distinct temporal dynamics and go vs. no-go preference. For most PFC$^{\rightarrow STN}$ neurons, the go cue elicited a transient excitation followed by decreasing activity throughout the delay period, whereas the no-go cue evoked slow but persistent upward ramping activity (Fig. 2*D*). In contrast, the majority of PFC$^{\rightarrow LH}$ neurons showed strong and sustained excitation in go but not no-go trials (Fig. 2*H*). To quantify the go vs. no-go preference of each neuron, we computed the difference between the trial-averaged activity in hit and CR trials, focusing on the late delay period that is most relevant to the motor response (Fig. 3 *A*–*D*). Of the 150 task-modulated PFC$^{\rightarrow STN}$ neurons, 94 showed significantly higher activity in CR than hit trials ($P < 0.05$, two-sided t test, CR-preferring), and only 8 were hit-preferring (Fig. 3*B*). In contrast, in the PFC$^{\rightarrow LH}$ population, hit-preferring neurons (73/123) greatly outnumbered CR-preferring neurons (19/123) (Fig. 3*D*).

We also compared trial-averaged activity between FA and CR trials and found 30 CR-preferring and only one FA-preferring PFC$^{\rightarrow STN}$ neurons (Fig. 3 *E* and *F*). In contrast, there were much fewer CR-preferring (4/123) than FA-preferring (40/123) PFC$^{\rightarrow LH}$ neurons (Fig. 3 *G* and *H*). Since FA and CR trials have the same auditory cue and differ only in the behavioral response, this indicates that PFC$^{\rightarrow STN}$ and PFC$^{\rightarrow LH}$ neurons have the opposite motor rather than sensory preferences.

Inputs to PFC$^{\rightarrow STN}$, PFC$^{\rightarrow V1}$, and PFC$^{\rightarrow LH}$ Neurons. To understand the circuit mechanism underlying the task-related activity of different dmPFC layer 5 neurons, we mapped the monosynaptic inputs to each population. AAV2-EF1α-DIO-TVA-eGFP and AAV8-FLEx-RG were injected into the dmPFC of *Rbp4^{Cre}* mice, and 3 wk later, rabies virus (RV) expressing tdTomato was injected into the STN, V1 or LH (Fig. 4*A*). This allowed RV to be taken up by the axon terminals in each region, expressed in the PFC$^{\rightarrow STN}$, PFC$^{\rightarrow V1}$, or PFC$^{\rightarrow LH}$ layer 5 neurons (Fig. 4*B*), and transsynaptically label their presynaptic inputs.

Although the three dmPFC populations receive inputs from largely overlapping brain areas (Fig. 4*D*), there are quantitative differences (Fig. 4 *C* and *D*). For example, compared to PFC$^{\rightarrow V1}$ and PFC$^{\rightarrow LH}$ neurons, PFC$^{\rightarrow STN}$ neurons receive stronger inputs

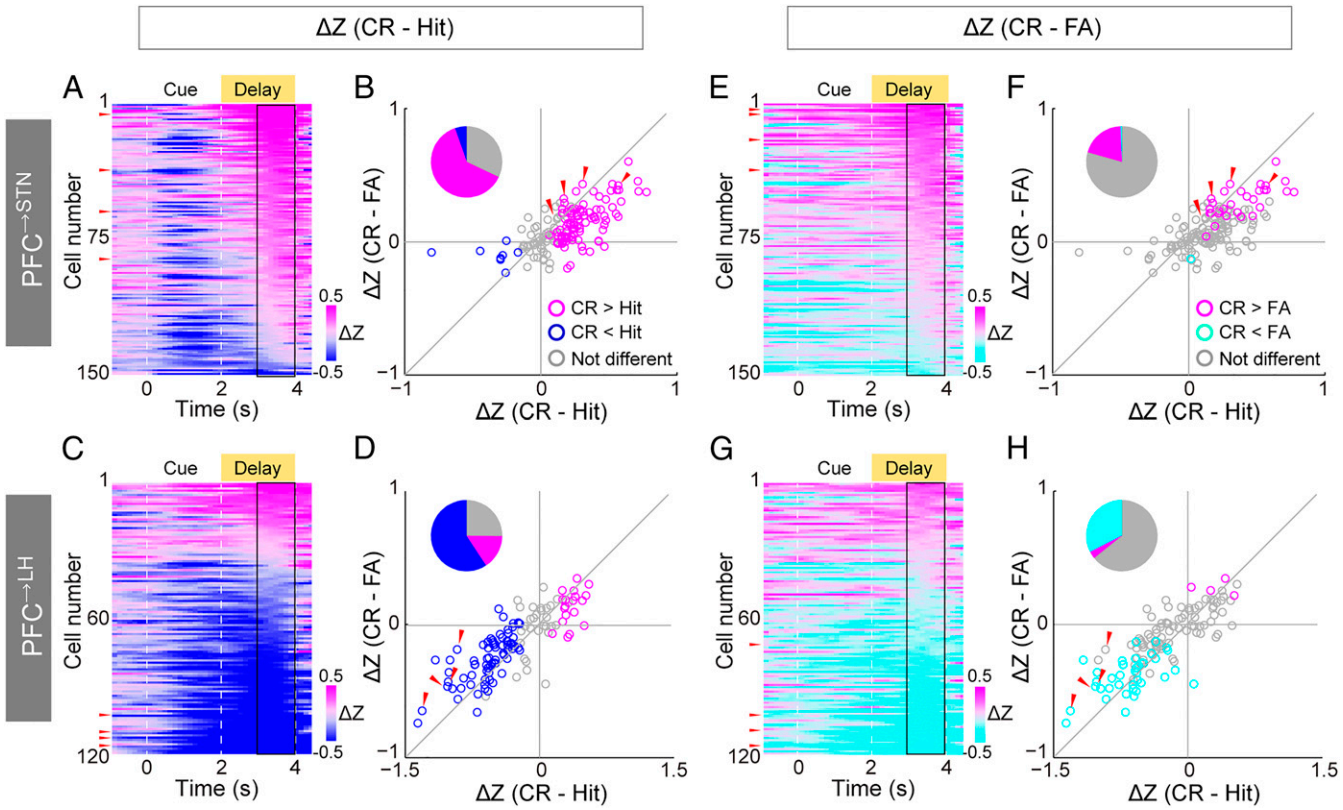

Fig. 3. Go vs. no-go preference of PFC$^{\rightarrow STN}$ and PFC$^{\rightarrow LH}$ neurons. (*A*) Color-coded difference between averaged Z-scored activity in CR and hit trials (CR – hit) for each PFC$^{\rightarrow STN}$ neuron. Neurons are sorted based on the averaged difference during the late delay period (3 to 4 s). Black rectangle indicates the late delay period quantified in *B*. Red arrows indicate the neurons shown in Fig. 2*D*. (*B*) CR – FA vs. CR – hit activity difference during the late delay period for PFC$^{\rightarrow STN}$ neurons. Magenta/blue circles indicate neurons with higher/lower activity in CR than hit trials ($P < 0.05$, two-sided t test). Red arrows indicate the neurons shown in Fig. 2*D*. (*C* and *D*) Similar to *A* and *B* but for PFC$^{\rightarrow LH}$ neurons. Red arrows indicate the neurons shown in Fig. 2*H*. (*E* and *F*) Similar to *A* and *B* but for the difference between CR and FA trials. (*G* and *H*) Similar to *E* and *F* but for PFC$^{\rightarrow LH}$ neurons.

Downloaded at Palestinian Territory, occupied on December 11, 2021

www.manaraa.com

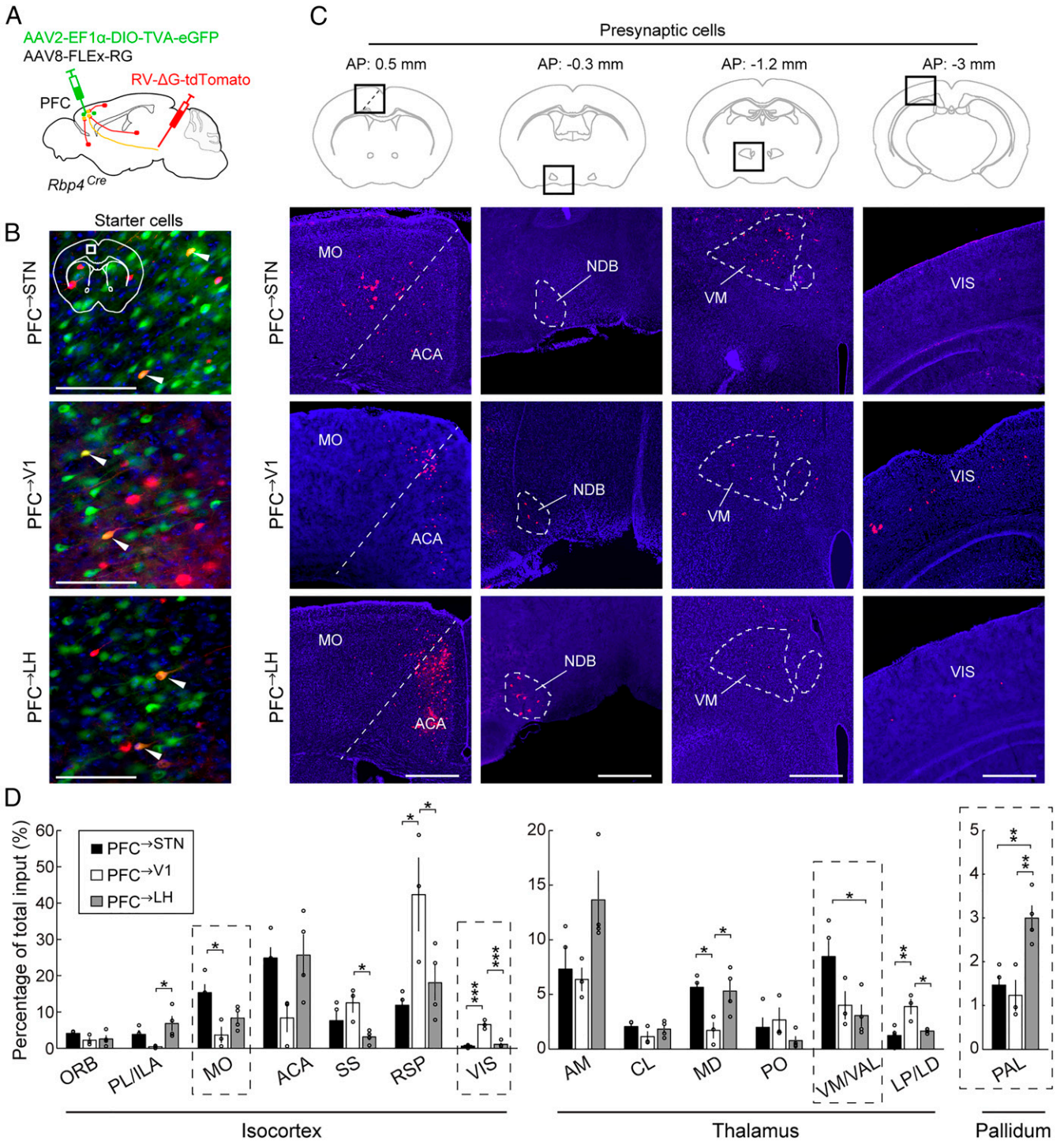

Fig. 4. Inputs to PFC$^{\rightarrow STN}$, PFC$^{\rightarrow V1}$, and PFC$^{\rightarrow LH}$ neurons. (*A*) Schematic for RV-mediated transsynaptic retrograde tracing. (*B*) Fluorescence images of starter cells in dmPFC (white box in coronal diagram). Red, RV-tdTomato; green, TVA-eGFP; blue, DAPI. White arrowheads indicate starter cells expressing both RV-tdTomato and TVA-eGFP. (Scale bar, 100 μm.) (*C*) Fluorescence images of presynaptic cells in several brain regions (black boxes in coronal diagrams). Red, RV-tdTomato; blue, DAPI. MO, somatomotor areas; ACA, anterior cingulate area; NDB, diagonal band nucleus; VM, ventral medial nucleus of the thalamus; VIS, visual cortical area. (Scale bar, 500 μm.) (*D*) Percentages of total presynaptic inputs (PFC$^{\rightarrow STN}$, $n = 4$ mice; PFC$^{\rightarrow V1}$, $n = 3$ mice; PFC$^{\rightarrow LH}$, $n = 4$ mice; $^{*}P < 0.05$; $^{**}P < 0.01$, $^{***}P < 0.001$, one-way ANOVA, Tukey's post hoc test). Only regions with >2% inputs to at least one of the three populations are shown. Dashed boxes indicate regions shown in *C*. ORB, orbital area; PL, prelimbic area; ILA, infralimbic area; SS, somatosensory areas; RSP, retrosplenial area; AM, anteromedial nucleus of the thalamus; CL, central lateral nucleus of the thalamus; MD, mediodorsal nucleus of the thalamus; PO, posterior complex of the thalamus; VAL, ventral anterior-lateral complex of the thalamus; LP, lateral posterior nucleus of the thalamus; LD, lateral dorsal nucleus of the thalamus. Error bars indicate ±SEM.

Downloaded at Palestinian Territory, occupied on December 11, 2021
www.manaraa.com

from the motor cortex (MO) and ventral anterior lateral complex (VAL) of the thalamus, both of which are essential areas for motor control (42). $PFC^{\rightarrow V1}$, but not $PFC^{\rightarrow LH}$ and $PFC^{\rightarrow STN}$ neurons, receive substantial inputs from V1 (43), consistent with reciprocity of corticocortical connections (44). $PFC^{\rightarrow LH}$ neurons, on the other hand, receive stronger inputs from the pallidum (PAL) (43), whose involvement in reward and motivation (45) may contribute to the strong activation of $PFC^{\rightarrow LH}$ neurons in go trials.

Causal Functions of $PFC^{\rightarrow STN}$ and $PFC^{\rightarrow LH}$ Neurons. To test the causal role of each dmPFC population in the go/no-go task, we injected rAAV2-retro-EF1α-DIO-ChR2 (41) into the STN, V1, or LH of $Rbp4^{Cre}$ mice (Fig. 5 *A* and *B* and *SI Appendix*, Fig. S3*A*). Laser stimulation was applied only during the delay and response periods of each trial to minimize the potential effect on cue perception. Activation of $PFC^{\rightarrow STN}$ neurons caused a marked improvement in task performance measured by correct rate ($P < 0.001$, bootstrap; *Materials and Methods*) by reducing the FA ($P < 0.001$) but not hit rate ($P = 0.77$; Fig. 5 *C* and *D*). In contrast, activating $PFC^{\rightarrow LH}$ neurons caused a significant behavioral impairment ($P = 0.04$) due to increased FA rate ($P = 0.03$; Fig. 5 *E* and *F*); activating $PFC^{\rightarrow V1}$ neurons had no significant effect (*SI Appendix*, Fig. S3*B*; correct rate, $P = 0.18$; hit rate, $P = 0.12$; FA rate, $P = 0.58$).

We then tested the effect of silencing each population through the light-activated chloride channel iC++ (46). Optogenetic inactivation of $PFC^{\rightarrow STN}$ neurons severely impaired the task performance (Fig. 5 *G* and *H*; correct rate, $P < 0.001$) by increasing the FA rate ($P < 0.001$), whereas inactivating $PFC^{\rightarrow LH}$ neurons improved the performance (Fig. 5 *I* and *J*; correct rate, $P = 0.04$) by decreasing the FA rate ($P = 0.04$). Interestingly, although $PFC^{\rightarrow STN}$ and $PFC^{\rightarrow LH}$ neurons strongly regulated the percentage of FA trials, their activation or inactivation had no effect on the motor execution of licking within hit or FA trials (*SI Appendix*, Fig. S4).

Function of the Hyperdirect Pathway. Since $PFC^{\rightarrow STN}$ neurons send axon collaterals to multiple brain regions, we tested the effect of activating their axon terminals in the STN. In $Rbp4^{Cre}$ mice injected with Cre-inducible AAV expressing the ChR2 variant ChETA (AAV2-EF1α-DIO-ChETA) (47) in the dmPFC (Fig. 6 *A* and *B*), 50-Hz laser stimulation at the STN caused a significant behavioral improvement (Fig. 6*C*; correct rate, $P = 0.03$; FA rate, $P < 0.001$), although no significant effect was observed with 10-Hz stimulation (*SI Appendix*, Fig. S5 *A* and *B*; correct rate, $P = 0.28$; FA rate, $P = 0.72$). In contrast, axon stimulation in V1 had no significant effect (*SI Appendix*, Fig. S3 *C* and *D*; correct rate, $P = 0.52$), and stimulation in the LH significantly impaired the performance (*SI Appendix*, Fig. S5 *C* and *D*; correct rate, $P = 0.006$; FA rate, $P = 0.01$), consistent with the effects of activating $PFC^{\rightarrow V1}$ and $PFC^{\rightarrow LH}$ cell bodies.

Stimulation of dmPFC axons in the STN could induce antidromic spiking and therefore activation of other collateral projections. To further examine the function of the PFC→STN pathway, we tested the effect of direct STN neuron activation. Since the peptide neurotensin (NTS) labels STN glutamatergic neurons (but not those in nearby structures) with a high specificity (*SI Appendix*, Fig. S6), we injected AAV2-EF1α-DIO-ChR2 into the STN of Nts^{Cre} mice (48) (Fig. 6 *D* and *E*). Laser stimulation at 10 Hz significantly improved the task performance ($P < 0.001$) by inducing a strong reduction of FA rate (−47.3 ± 4.6%, SEM) but a much weaker reduction of hit rate (−8.8 ± 3.0%; Fig. 6*F* and *SI Appendix*, Fig. S7 *A* and *B*). This supports the hypothesis that inhibition of inappropriate responses by $PFC^{\rightarrow STN}$ neurons is at least partly mediated by their excitation of STN neurons through the hyperdirect pathway.

Discussion

Using projection-specific labeling and calcium imaging, we have shown that STN- but not V1- or LH-projecting dmPFC layer 5 neurons are preferentially active when the animal withholds a prepotent licking response. Optogenetic activation and inactivation showed that activity of $PFC^{\rightarrow STN}$ neurons improves response inhibition, but $PFC^{\rightarrow LH}$ neuron activity is detrimental to the task performance. The effect of $PFC^{\rightarrow STN}$ neurons is mediated at least in part by the hyperdirect pathway.

Unlike the entire layer 5 population, which contains go-preferring, NG-preferring, and weakly modulated neurons (Fig. 2), an overwhelming majority of the $PFC^{\rightarrow STN}$ subpopulation are NG-preferring (Fig. 3), suggesting a specialized role in inhibiting habitual responses, a function known to depend on the medial frontal cortex (49, 50). In contrast, $PFC^{\rightarrow LH}$ neurons are more heterogeneous; although their activation causes an impairment of response inhibition (Fig. 5), a small but significant fraction of the neurons are NG-preferring. Given the ∼10% overlap between $PFC^{\rightarrow LH}$ and $PFC^{\rightarrow STN}$ neurons (Fig. 1*E*, which is likely an underestimate due to incomplete retrograde labeling of each population), some of the NG-preferring $PFC^{\rightarrow LH}$ neurons may also project to the STN. In addition to the $PFC^{\rightarrow STN}$ layer 5 population, dmPFC neurons projecting to the basal ganglia indirect pathway (i.e., innervating striatal neurons expressing D2 dopamine receptors) may also contribute to response inhibition (51).

The weak task-dependent modulation of $PFC^{\rightarrow V1}$ neurons (Fig. 2*F*) and the lack of effect of their activation on behavioral performance (*SI Appendix*, Fig. S3*B*) are not surprising, because the task used in this study does not require visual processing. However, the behavioral effects of manipulating $PFC^{\rightarrow LH}$ neurons (Fig. 5 *E*, *F*, *I*, and *J*) were unexpected. The improvement induced by their inactivation suggests that the nonoptimal task performance is partly due to overactivation or insufficient inhibition of $PFC^{\rightarrow LH}$ neurons, which may drive inappropriate reward-seeking by activating LH GABAergic neurons (40). $PFC^{\rightarrow LH}$ neuron activity could be modulated by long-range inputs from numerous brain regions (Fig. 4); given the opposing functions of $PFC^{\rightarrow STN}$ and $PFC^{\rightarrow LH}$ neurons observed in this study, it is also possible that the two populations inhibit each other through local GABAergic interneurons.

The STN is well known to be important for response inhibition (26–33). In the current task it is likely to receive stronger excitation from $PFC^{\rightarrow STN}$ neurons in no-go than go trials (Fig. 3 *A* and *B*). Notably, optogenetic activation of STN neurons with 10-Hz laser stimulation improved task performance even when applied in both go and no-go trials (Fig. 6*F*). However, a much stronger activation at 50 Hz caused a severe impairment, due to a near-complete suppression of licking in all trials (*SI Appendix*, Fig. S7 *C–E*; $P < 0.001$ for correct, hit, and FA rates). Such a general suppression is consistent with a recent study (52), presumably mediated by a strong excitation of the internal segment of the globus pallidus (GPi) and substantia nigra pars reticulata (SNr), which broadly inhibit multiple motor circuits (33, 42, 51). With moderate STN activation, however, the excitation of GPi/SNr may be overridden by a strong inhibition elicited by the go cue, resulting in selective sparing of hit rate (*SI Appendix*, Fig. S7 *A* and *B*).

A prominent feature of the PFC is functional diversity among neighboring pyramidal neurons (11–14). In addition to laminar differences (6, 15), a high degree of heterogeneity in go vs. no-go preference was observed within layer 5 of the dmPFC, similar to that in the motor cortex (16). Here we show that a subset of pyramidal neurons—defined by both their layer 5 laminar identity and projection to the STN—exhibit strong functional homogeneity regarding response inhibition. This provides an

NEUROSCIENCE

Downloaded at Palestinian Territory, occupied on December 11, 2021
www.manaraa.com

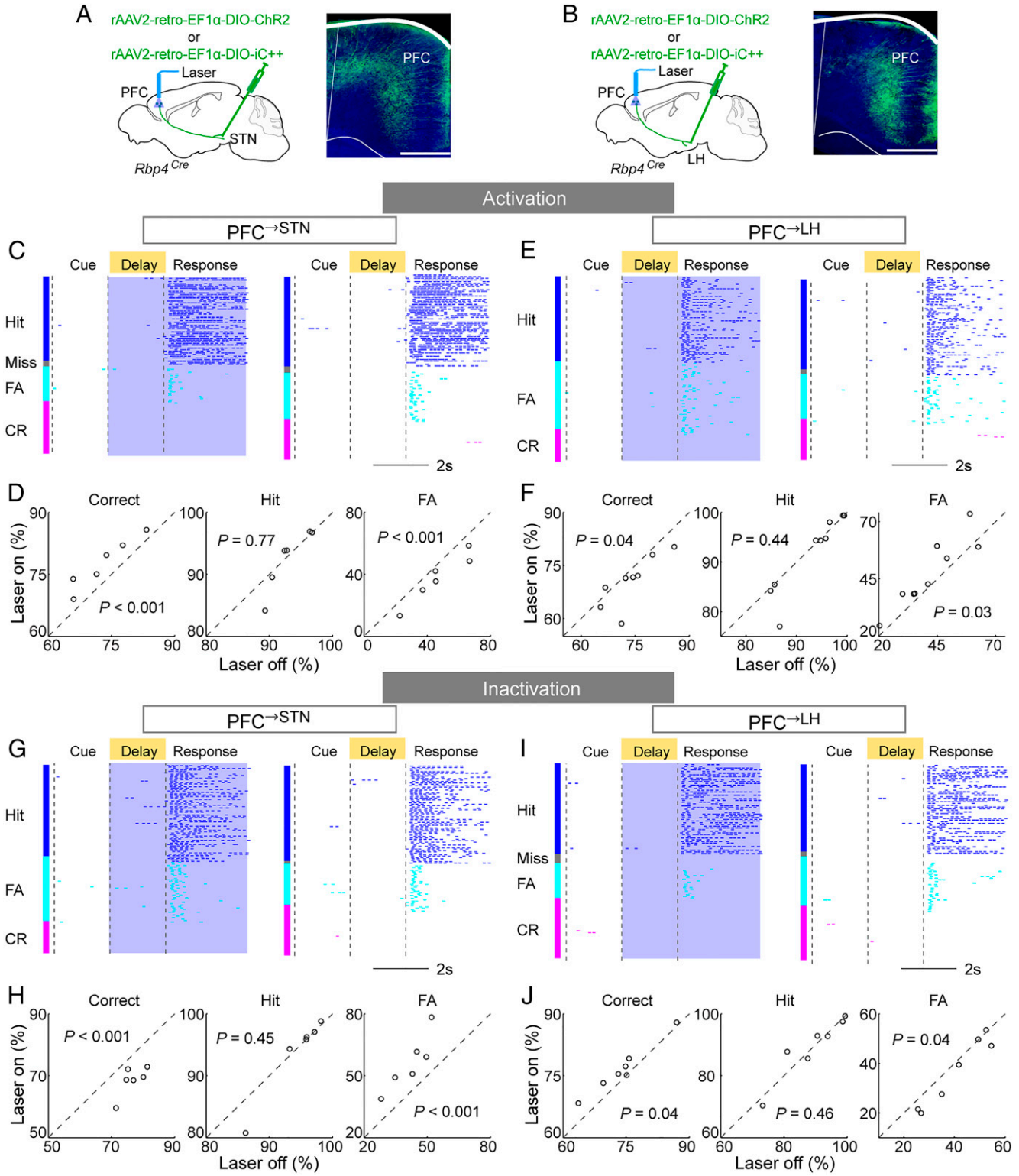

Fig. 5. Causal functions of PFC$^{\rightarrow STN}$ and PFC$^{\rightarrow LH}$ neurons. (*A*) Schematic of optogenetic activation/inactivation of PFC$^{\rightarrow STN}$ neurons (*Left*) and fluorescence image of dmPFC expressing ChR2-eYFP (*Right*). Green, ChR2-eYFP; blue, DAPI. (Scale bar, 400 μm.) (*B*) Similar to *A* but for PFC$^{\rightarrow LH}$ neurons. (*C*) An example session with PFC$^{\rightarrow STN}$ neuron activation. (*Left*) Laser on trials and (*Right*) laser off trials. Blue shading indicates laser stimulation. Each tick indicates one lick. (*D*) Activation of PFC$^{\rightarrow STN}$ neurons caused a marked improvement in task performance by reducing the FA rate (correct rate, $P < 0.001$; hit rate, $P = 0.77$; FA rate, $P < 0.001$; bootstrap). Each circle represents one mouse ($n = 6$ mice). (*E* and *F*) Similar to *C* and *D* but for behavioral impairment caused by PFC$^{\rightarrow LH}$ neuron activation (correct rate, $P = 0.04$; hit rate, $P = 0.44$; FA rate, $P = 0.03$; $n = 9$ mice). (*G* and *H*) Similar to *C* and *D* but for PFC$^{\rightarrow STN}$ neuron inactivation (correct rate, $P < 0.001$; hit rate, $P = 0.45$; FA rate, $P < 0.001$; $n = 6$ mice). (*I* and *J*) Similar to *G* and *H* but for PFC$^{\rightarrow LH}$ neuron inactivation (correct rate, $P = 0.04$; hit rate, $P = 0.46$; FA rate, $P = 0.04$; $n = 7$ mice).

Downloaded at Palestinian Territory, occupied on December 11, 2021
www.manaraa.com

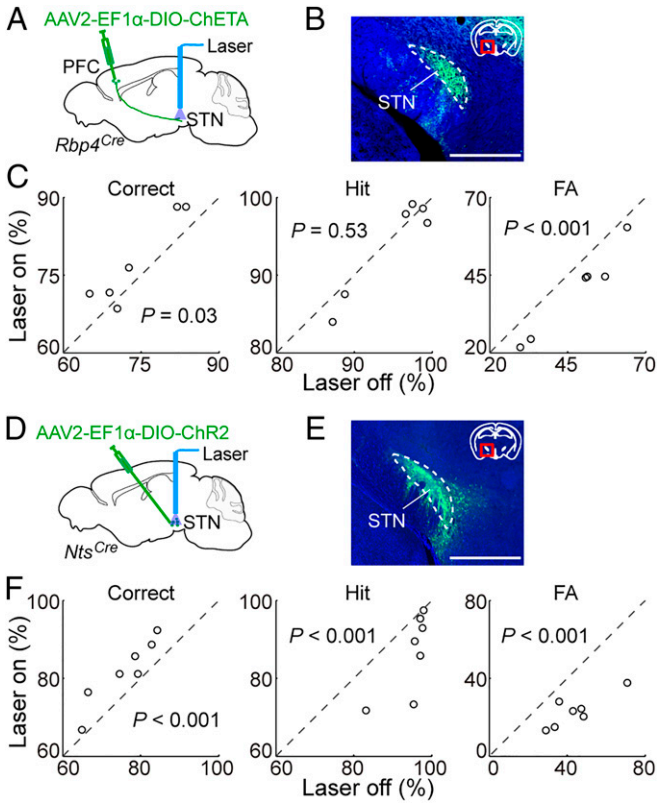

Fig. 6. Effects of activating PFC$^{\rightarrow STN}$ axons or STN neurons. (*A*) Schematic of optogenetic activation of dmPFC axon terminals in STN. (*B*) Fluorescence image showing ChETA-eYFP expressing dmPFC axons in STN. Green, ChETA-eYFP; blue, DAPI. (Scale bar, 1 mm.) (*C*) Activation of dmPFC axon terminals in STN (50 Hz) caused a significant improvement in task performance by reducing the FA rate (correct rate, $P = 0.03$; hit rate, $P = 0.53$; FA rate, $P < 0.001$; bootstrap, $n = 6$ mice). (*D*) Schematic of optogenetic activation of STN cells. (*E*) Fluorescence image showing ChR2-eYFP expression in STN neurons. Green, ChR2-eYFP; blue, DAPI. (Scale bar, 1 mm.) (*F*) Activation of STN cell (10 Hz) caused a significant improvement in task performance (correct, hit, and FA rates are all $P < 0.001$; bootstrap, $n = 7$ mice).

important entry point for delineating the PFC circuit underlying impulse control.

Materials and Methods

Animals. *Rbp4*^{Cre} (GENSAT, 031125-UCD) was obtained from GENSAT and *Nts*^{Cre} (Jackson, 017525) was obtained from Jackson Laboratory. Experiments were performed in adult mice (2-6 mo old) of both genders. Mice were group-housed before surgery and single-housed after they were implanted with GRIN lenses or optical fibers. Mice were housed in 12-h light–dark cycle (lights on at 07:00 AM and off at 07:00 PM) with free access to food and water outside of the training and testing period. All procedures were approved by the Animal Care and Use Committees of the University of California, Berkeley.

Virus Preparation. AAV2-EF1α-DIO-ChR2-eYFP, AAV2-EF1α-DIO-mCherry, AAV2-EF1α-DIO-ChETA-eYFP, and AAV8-FLEx-RG (RG, rabies glycoprotein) were obtained from the University of North Carolina (~5×10^{12} genome copies [gc]/mL) vector core. AAV2-EF1α-DIO-TVA-eGFP (~5×10^{12} gc/mL), rAAV2-retro-EF1α-DIO-GCaMP6s (~10^{13} gc/mL, but diluted 5 times before injection), rAAV2-retro-EF1α-DIO-ChR2-eYFP (~5×10^{12} gc/mL), rAAV2-retro-EF1α-DIO-iC++-eYFP (~5×10^{12}gc/mL), rAAV2-retro-EF1α-DIO-mCherry (~5×10^{12} gc/mL), and rAAV2-retro-EF1α-DIO-eGFP (~5×10^{12} gc/mL) were packaged in house according to previously described protocols (43, 53). RG-deleted, tdTomato-expressing rabies virus (RV-ΔG-tdTomato, ~1.5×10^{9} IU/mL) was amplified in B7GG cells, pseudotyped with BHK-EnvA cells, and titered with HEK293-TVA cells (54). RV-ΔG-tdTomato was a gift from B. Lim at University of California San Diego, La Jolla, CA. B7GG cells, BHK-EnvA, cells and HEK293-TVA cells were gifts from E. Callaway at the Salk Institute for Biological Studies, La Jolla, CA.

Surgical Procedures. Adult mice (2 to 6 mo old) were anesthetized with isoflurane (5% induction and 1.5% maintenance) and placed on a stereotaxic frame (David Kopf Instruments). Body temperature was kept stable throughout the procedure using a heating pad. Eye ointment was applied to keep the eyes from drying. Mice of specific genotype were randomly assigned to experimental groups. Investigators were not blinded to animal identity and outcome assessment.

For anterograde tracing and dual retrograde labeling experiments, a craniotomy was made on top of the target regions (see below for coordinates), 0.1 to 0.3 μL virus was injected into the target regions using Nanoject II (Drummond Scientific), and mice were sacrificed 3 wk later for histology. For rabies-mediated retrograde transsynaptic tracing experiments, a mixture of AAV2-EF1α-DIO-TVA-eGFP and AAV8-FLEx-RG (~0.3 μL) was injected into dmPFC. Three weeks later, RV-ΔG-tdTomato was injected into STN, V1, or LH, and mice were sacrificed 7 d later for histology.

For imaging experiments, 0.3 to 0.5 μL virus was injected into each target region. A stainless steel headplate was then affixed to the skull. The region surrounding the craniotomy was protected with a silicone elastomer (Kwik-Cast; World Precision Instruments). After a week of recovery, the mice underwent the initial stages of behavioral training (habituation and conditioning) for ~2 wk, and a second surgical procedure was performed to implant the GRIN lens (diameter, 1 mm; length, 4.2 mm; pitch, 0.5; numerical aperture, 0.5; Inscopix) to target the dmPFC (6, 15).

For optogenetic activation/inactivation experiments, 0.3 to 0.5 μL virus was injected into the target region. Two weeks after viral injection, optic fibers (0.2 mm diameter; Thorlabs) were implanted with the tip 0.2 mm above the target region. A stainless steel headplate was affixed to the skull, and dental cement was applied to cover the exposed skull completely and to secure the implants for behavioral training.

Stereotaxic coordinates for virus injection, GRIN lens and optic fiber implantation are as follows: dmPFC, anteroposterior (AP) 1 mm, mediolateral (ML) 0.5 mm, dorsoventral (DV) 0.8 mm; STN, AP −1.8 mm, ML 1.6 mm, DV 4.7 mm; LH, AP −1 mm, ML 0.6 mm, DV 5.1 mm; and V1, AP −3 mm, ML 2.5 mm, DV 0.5 mm.

Behavioral Procedures. We trained head-fixed mice on a delayed go/no-go auditory task, including habituation, conditioning, and discrimination phases (6). In the habituation phase, the mouse was given free water rewards (~4 μL) for each lick. In the conditioning phase, the mouse was trained to lick in response to a target tone stimulus (17 kHz, 65 dB), which lasted for 2 s in each trial. The mouse was advanced to the next phase once the number of licks exceeded 150 within 30 min. In the discrimination phase, each trial started either with the target or nontarget (9 kHz, 65 dB) tone (in go or no-go trials, respectively). The auditory stimulus (cue period) lasted for 2 s, followed by a delay period (which increased gradually from 0 to 2 s over multiple training sessions; see below). A water port was presented after the delay. Licking in response to a target tone (hit) within the first 2 s after the water port presentation (response window) was rewarded with a drop of water delivered through the water port, while licking in response to a nontarget tone (FA) triggered a combination of electric shock at the tip of the tongue (less than 1 mA), airpuff to the cheek (15 to 20 psi, 200 ms), and 7-s timeout period. No licking in response to a target or nontarget tone within the response window was regarded as a miss or correct rejection (CR) trial, respectively. Licking outside of the response window had no consequence. The water port was retracted after 3 s from the first lick in hit and FA trials or 2 s after the end of the response window in miss and CR trials. The intertrial interval was 7.5 s. All licks were detected by an infrared beam-break lickometer. The delay period was gradually increased from 0 to 2 s in 500-ms steps when behavioral performance reached ~70% correct in a 50-trial block. Mice were trained daily (one session per day, ~300 trials per session, except for a ~4-d break for GRIN lens implantation) until reaching criterion performance, defined as >70% correct trials for at least 3 consecutive days or >75% correct for 2 consecutive days. These criteria were chosen to avoid overtraining prior to the experimental manipulations, while ensuring above-chance performance. Mice were water restricted and ordinarily had access to water only during training. However, additional water was given if necessary to ensure that their body weight (monitored daily) did not drop below 85% of the starting value. Once the mice reached these criteria, we started performing calcium imaging experiments or optogenetic manipulation experiments.

Downloaded at Palestinian Territory, occupied on December 11, 2021

www.manaraa.com

Two-Photon Calcium Imaging. Two-photon calcium imaging was performed using a custom two-photon microscope that has been described previously (55). In brief, the microscope (Movable Objective Microscope; Sutter Instrument) was controlled by the ScanImage software (56) and the objective was a 20× water immersion lens (*XLUMPlanFI*, 0.95 NA; Olympus). Excitation intensity from a tunable femtosecond laser (Wideband, Tsunami Mode-Locked Ti:Sapphire Laser; Spectra-Physics) was controlled by a Pockels cell (350-80-LA-02; Conoptics). GCaMP6s was excited at 920 nm, and fluorescence emission was collected using a GaAsP PMT (H10770PA-40; Hamamatsu). Images (128 × 128 pixels) were acquired at ∼6.73 Hz.

Optogenetic Manipulation. Optic fibers (200 μm diameter; ThorLabs) were attached to a 473-nm blue laser diode (Shanghai laser), and light pulses were generated under the control of a Master 8 (A.M.P.I.). Optogenetic activation experiments were performed unilaterally, and optogenetic inhibition experiments were performed bilaterally. Laser stimulation started at the delay period onset and continued for 5 s (covering the delay period, the response window, and 1 s after response window) in each trial. Light pulses (5 ms per pulse, 10 or 50 Hz) were applied for optogenetic activation experiments. The laser power was 1 to 2 mW or ∼10 mW at fiber tip for cell body activation or terminal activation experiments, respectively. For optogenetic inactivation experiments, constant light (∼5 mW) was used. Unless otherwise stated, laser stimulation was applied in 50% of pseudorandomly selected trials, but the same condition never occurred in more than five consecutive trials. In STN cell body activation experiments with 50-Hz pulse train, laser stimulation was applied in 25% of trials to reduce negative effect on the motivation to perform the task. Each experimental session lasted for ∼1 h, and each animal was tested for five to eight sessions.

Calcium Imaging Data Analyses. The brain motion was corrected by a custom MATLAB script using an open source toolkit ANTs (57–59) (picsl.upenn.edu/software/ants/). Regions of interest (ROIs) corresponding to identifiable cell bodies were selected using the SD projection of the motion-corrected video using ImageJ (23) and a pixel-wise activity map (15, 60). The pixels within each ROI were averaged to create a fluorescence time series. The baseline fluorescence of the ROI, F_0, was estimated as the eighth percentile (61) of the fluorescence in a ±60-s window and used to calculate $\Delta F/F_0 = ((F - F_0)/F_0)$. Unless otherwise stated, $\Delta F/F_0$ traces were Z scored.

To assess whether a neuron was significantly modulated by the task, we performed a two-way ANOVA with factors trial type (Hit, CR, and FA) and epoch (1 s before cue, cue, and delay). A neuron was deemed significantly modulated if $P < 0.01$ for at least one of the factors or interaction terms. Unless otherwise stated, trials were excluded if lick happened during the delay period. Miss trials were not considered as the numbers of miss trials were very small in most cases.

To quantify the separability between the population activity in the correct go (hit) and no-go (CR) trials, we computed the Euclidean distance for trial-averaged Z-score traces of a population of neurons. Ten neurons were randomly selected in each imaging session. The Euclidean distances in these neurons were computed for each time point between hit trials and CR trials and then normalized by the mean distance during the baseline period (1 s before cue onset). We repeated this procedure 1,000 times to get the averaged distance. Statistical significance was determined using Wilcoxon rank sum test ($P < 0.05$ as the criterion).

Response preference was quantified during the late delay period (3 to 4 s after cue onset) based on Z-scored traces averaged within each trial type for each neuron. A neuron with higher/lower activity in CR trials than in hit trials ($P < 0.05$, two-sided t test) was defined as a CR/hit-preferring neuron. Similar comparison was performed between FA and CR trials.

Behavioral Data Analyses. Correct rate, hit rate, and FA rate were quantified as follows:

$$\text{Correct rate} = (\text{number of Hits} + \text{number of CRs})/\text{total number of trials}*100,$$

$$\text{Hit rate} = \text{number of Hits}/(\text{number of Hits} + \text{number of Misses})*100,$$

$$\text{FA rate} = \text{number of FAs}/(\text{number of FAs} + \text{number of CRs})*100.$$

Significance of the behavioral effects caused by optogenetic manipulation was determined using bootstrap (22, 62–64). Briefly, in each iteration we resampled the original data with replacement from 1) animals, 2) sessions performed by each animal, and 3) the trials within each session. We then computed the performance change on the resampled dataset. This procedure was repeated 10,000 times to obtain a distribution of performance changes. The P value was computed as the fraction of times the bootstrapping produced an inconsistent performance change.

Immunohistochemistry and Fluorescence In Situ Hybridization. Mice were deeply anesthetized and transcardially perfused with 0.1 M PBS followed by 4% paraformaldehyde in PBS. Brains were kept overnight in 4% paraformaldehyde for fixation and then in 30% sucrose in PBS solution for 36 to 48 h for cryoprotection. After embedding and freezing, brains were sectioned into 30-μm (for fluorescence in situ hybridization [FISH]) or 50-μm coronal slices using a cryostat. For immunohistochemistry, brain slices were washed using PBS three times, permeabilized using PBST (0.3% Triton X-100 in PBS) for 30 min, and then incubated with blocking solution (5% normal goat serum or normal donkey serum in PBST) for 1 h, followed by primary antibody incubation overnight at 4 °C using anti-RPF antibody (600-401-379, Rockland; 1:1,000). The next day, slices were washed three times with PBS, incubated with the secondary antibody (Donkey anti-Rabbit IgG, Alexa Fluor 594, A-21207, Invitrogen; 1:1,000) for 2 h. To determine overlap between *Nts* and *Slc17a6*, dual FISH was done using RNAscope assays according to the manufacturer's instructions (Advanced Cell Diagnostics). Fluorescence images were acquired using a high-throughput slide scanner (Nanozoomer-2.0RS; Hamamatsu) and a fluorescence microscope (Keyence, BZ-X710).

Statistics. All statistical analysis was performed using MATLAB. Unless otherwise stated, data are presented as mean ± SEM. Statistical method, statistic, and corresponding P values are reported in the figure legends.

Data Availability Statement. All relevant data are included in the manuscript and *SI Appendix*.

ACKNOWLEDGMENTS. We thank Zhe Zhang, Danqian Liu, and Kai-Siang Chen for sharing the virus for the retrograde tracing and rabies virus tracing experiments; Lucas Pinto and Tsukasa Kamigaki for providing programs for data analysis; and Yaxuan Zhou, Jing Zhang, and Fei Hu for help with behavioral training. This work was supported by the Howard Hughes Medical Institute.

1. J. M. Fuster, *The Prefrontal Cortex*, (Academic, Amsterdam, ed. 4, 2008).
2. A. Bari, T. W. Robbins, Inhibition and impulsivity: Behavioral and neural basis of response control. *Prog. Neurobiol.* **108**, 44–79 (2013).
3. A. Sebastian *et al*., Frontal dysfunctions of impulse control—A systematic review in borderline personality disorder and attention-deficit/hyperactivity disorder. *Front. Hum. Neurosci.* **8**, 698 (2014).
4. S. D. Iversen, M. Mishkin, Perseverative interference in monkeys following selective lesions of the inferior prefrontal convexity. *Exp. Brain Res.* **11**, 376–386 (1970).
5. H. Eichenbaum, R. A. Clegg, A. Feeley, Reexamination of functional subdivisions of the rodent prefrontal cortex. *Exp. Neurol.* **79**, 434–451 (1983).
6. T. Kamigaki, Y. Dan, Delay activity of specific prefrontal interneuron subtypes modulates memory-guided behavior. *Nat. Neurosci.* **20**, 854–863 (2017).
7. L. M. Broersen, H. B. Uylings, Visual attention task performance in Wistar and Lister hooded rats: Response inhibition deficits after medial prefrontal cortex lesions. *Neuroscience* **94**, 47–57 (1999).
8. C. Risterucci, D. Terramorsi, A. Nieoullon, M. Amalric, Excitotoxic lesions of the prelimbic-infralimbic areas of the rodent prefrontal cortex disrupt motor preparatory processes. *Eur. J. Neurosci.* **17**, 1498–1508 (2003).
9. N. S. Narayanan, M. Laubach, Top-down control of motor cortex ensembles by dorsomedial prefrontal cortex. *Neuron* **52**, 921–931 (2006).
10. S. Hardung *et al*., A functional gradient in the rodent prefrontal cortex supports behavioral inhibition. *Curr. Biol.* **27**, 549–555 (2017).
11. D. R. Euston, A. J. Gruber, B. L. McNaughton, The role of medial prefrontal cortex in memory and decision making. *Neuron* **76**, 1057–1070 (2012).
12. E. K. Miller, J. D. Cohen, An integrative theory of prefrontal cortex function. *Annu. Rev. Neurosci.* **24**, 167–202 (2001).
13. C. K. Machens, R. Romo, C. D. Brody, Functional, but not anatomical, separation of "what" and "when" in prefrontal cortex. *J. Neurosci.* **30**, 350–360 (2010).
14. M. Rigotti *et al*., The importance of mixed selectivity in complex cognitive tasks. *Nature* **497**, 585–590 (2013).
15. L. Pinto, Y. Dan, Cell-type-specific activity in prefrontal cortex during goal-directed behavior. *Neuron* **87**, 437–450 (2015).
16. E. Zagha, X. Ge, D. A. McCormick, Competing neural ensembles in motor cortex gate goal-directed motor output. *Neuron* **88**, 565–577 (2015).
17. T. Yamashita *et al*., Membrane potential dynamics of neocortical projection neurons driving target-specific signals. *Neuron* **80**, 1477–1490 (2013).

Downloaded at Palestinian Territory, occupied on December 11, 2021
www.manaraa.com

18. L. L. Glickfeld, M. L. Andermann, V. Bonin, R. C. Reid, Cortico-cortical projections in mouse visual cortex are functionally target specific. *Nat. Neurosci.* **16**, 219–226 (2013).
19. J. L. Chen, S. Carta, J. Soldado-Magraner, B. L. Schneider, F. Helmchen, Behaviour-dependent recruitment of long-range projection neurons in somatosensory cortex. *Nature* **499**, 336–340 (2013).
20. B. Jarosiewicz, J. Schummers, W. Q. Malik, E. N. Brown, M. Sur, Functional biases in visual cortex neurons with identified projections to higher cortical targets. *Curr. Biol.* **22**, 269–277 (2012).
21. M. N. Economo *et al*., Distinct descending motor cortex pathways and their roles in movement. *Nature* **563**, 79–84 (2018).
22. N. Li, T. W. Chen, Z. V. Guo, C. R. Gerfen, K. Svoboda, A motor cortex circuit for motor planning and movement. *Nature* **519**, 51–56 (2015).
23. J. M. Otis *et al*., Prefrontal cortex output circuits guide reward seeking through divergent cue encoding. *Nature* **543**, 103–107 (2017).
24. M. Murugan *et al*., Combined social and spatial coding in a descending projection from the prefrontal cortex. *Cell* **171**, 1663–1677.e16 (2017).
25. C. K. Kim *et al*., Molecular and circuit-dynamical identification of top-down neural mechanisms for restraint of reward seeking. *Cell* **170**, 1013–1027.e14 (2017).
26. M. J. Frank, J. Samanta, A. A. Moustafa, S. J. Sherman, Hold your horses: Impulsivity, deep brain stimulation, and medication in parkinsonism. *Science* **318**, 1309–1312 (2007).
27. D. M. Eagle *et al*., Stop-signal reaction-time task performance: Role of prefrontal cortex and subthalamic nucleus. *Cereb. Cortex* **18**, 178–188 (2008).
28. J. F. Cavanagh *et al*., Subthalamic nucleus stimulation reverses mediofrontal influence over decision threshold. *Nat. Neurosci.* **14**, 1462–1467 (2011).
29. C. Baunez, T. W. Robbins, Bilateral lesions of the subthalamic nucleus induce multiple deficits in an attentional task in rats. *Eur. J. Neurosci.* **9**, 2086–2099 (1997).
30. M. Isoda, O. Hikosaka, Role for subthalamic nucleus neurons in switching from automatic to controlled eye movement. *J. Neurosci.* **28**, 7209–7218 (2008).
31. A. R. Aron, R. A. Poldrack, Cortical and subcortical contributions to stop signal response inhibition: Role of the subthalamic nucleus. *J. Neurosci.* **26**, 2424–2433 (2006).
32. A. R. Aron, D. M. Herz, P. Brown, B. U. Forstmann, K. Zaghloul, Frontosubthalamic circuits for control of action and cognition. *J. Neurosci.* **36**, 11489–11495 (2016).
33. R. Schmidt, D. K. Leventhal, N. Mallet, F. Chen, J. D. Berke, Canceling actions involves a race between basal ganglia pathways. *Nat. Neurosci.* **16**, 1118–1124 (2013).
34. A. Nambu, H. Tokuno, M. Takada, Functional significance of the cortico-subthalamo-pallidal "hyperdirect" pathway. *Neurosci. Res.* **43**, 111–117 (2002).
35. T. Kita, H. Kita, The subthalamic nucleus is one of multiple innervation sites for long-range corticofugal axons: A single-axon tracing study in the rat. *J. Neurosci.* **32**, 5990–5999 (2012).
36. G. M. Shepherd, Corticostriatal connectivity and its role in disease. *Nat. Rev. Neurosci.* **14**, 278–291 (2013).
37. C. R. Gerfen, R. Paletzki, N. Heintz, GENSAT BAC cre-recombinase driver lines to study the functional organization of cerebral cortical and basal ganglia circuits. *Neuron* **80**, 1368–1383 (2013).
38. D. G. R. Tervo *et al*., A designer AAV variant permits efficient retrograde access to projection neurons. *Neuron* **92**, 372–382 (2016).
39. S. Zhang *et al*., Selective attention. Long-range and local circuits for top-down modulation of visual cortex processing. *Science* **345**, 660–665 (2014).
40. J. H. Jennings *et al*., Visualizing hypothalamic network dynamics for appetitive and consummatory behaviors. *Cell* **160**, 516–527 (2015).
41. K. S. Chen *et al*., A hypothalamic switch for REM and non-REM sleep. *Neuron* **97**, 1168–1176.e4 (2018).
42. A. Parent, L. N. Hazrati, Functional anatomy of the basal ganglia. I. The cortico-basal ganglia-thalamo-cortical loop. *Brain Res. Brain Res. Rev.* **20**, 91–127 (1995).
43. S. Zhang *et al*., Organization of long-range inputs and outputs of frontal cortex for top-down control. *Nat. Neurosci.* **19**, 1733–1742 (2016).
44. S. W. Oh *et al*., A mesoscale connectome of the mouse brain. *Nature* **508**, 207–214 (2014).
45. K. S. Smith, A. J. Tindell, J. W. Aldridge, K. C. Berridge, Ventral pallidum roles in reward and motivation. *Behav. Brain Res.* **196**, 155–167 (2009).
46. A. Berndt *et al*., Structural foundations of optogenetics: Determinants of channelrhodopsin ion selectivity. *Proc. Natl. Acad. Sci. U.S.A.* **113**, 822–829 (2016).
47. L. A. Gunaydin *et al*., Ultrafast optogenetic control. *Nat. Neurosci.* **13**, 387–392 (2010).
48. G. M. Leinninger *et al*., Leptin action via neurotensin neurons controls orexin, the mesolimbic dopamine system and energy balance. *Cell Metab.* **14**, 313–323 (2011).
49. M. Isoda, O. Hikosaka, Switching from automatic to controlled action by monkey medial frontal cortex. *Nat. Neurosci.* **10**, 240–248 (2007).
50. C. A. Duan, J. C. Erlich, C. D. Brody, Requirement of prefrontal and midbrain regions for rapid executive control of behavior in the rat. *Neuron* **86**, 1491–1503 (2015).
51. C. R. Gerfen, D. J. Surmeier, Modulation of striatal projection systems by dopamine. *Annu. Rev. Neurosci.* **34**, 441–466 (2011).
52. K. H. Fife *et al*., Causal role for the subthalamic nucleus in interrupting behavior. *eLife* **6**, e27689 (2017).
53. W. W. Hauswirth, A. S. Lewin, S. Zolotukhin, N. Muzyczka, "Production and purification of recombinant adeno-associated virus" in *Methods in Enzymology*, K. Palczewski, Ed. (Academic Press, 2000), Vol. 316, pp. 743–761.
54. F. Osakada, E. M. Callaway, Design and generation of recombinant rabies virus vectors. *Nat. Protoc.* **8**, 1583–1601 (2013).
55. Y. Li *et al*., Clonally related visual cortical neurons show similar stimulus feature selectivity. *Nature* **486**, 118–121 (2012).
56. T. A. Pologruto, B. L. Sabatini, K. Svoboda, ScanImage: Flexible software for operating laser scanning microscopes. *Biomed. Eng. Online* **2**, 13 (2003).
57. B. B. Avants, C. L. Epstein, M. Grossman, J. C. Gee, Symmetric diffeomorphic image registration with cross-correlation: Evaluating automated labeling of elderly and neurodegenerative brain. *Med. Image Anal.* **12**, 26–41 (2008).
58. J. N. Betley *et al*., Neurons for hunger and thirst transmit a negative-valence teaching signal. *Nature* **521**, 180–185 (2015).
59. J. Cox, L. Pinto, Y. Dan, Calcium imaging of sleep-wake related neuronal activity in the dorsal pons. *Nat. Commun.* **7**, 10763 (2016).
60. M. B. Ahrens *et al*., Brain-wide neuronal dynamics during motor adaptation in zebrafish. *Nature* **485**, 471–477 (2012).
61. C. D. Harvey, P. Coen, D. W. Tank, Choice-specific sequences in parietal cortex during a virtual-navigation decision task. *Nature* **484**, 62–68 (2012).
62. Z. Gao *et al*., A cortico-cerebellar loop for motor planning. *Nature* **563**, 113–116 (2018).
63. Z. V. Guo *et al*., Flow of cortical activity underlying a tactile decision in mice. *Neuron* **81**, 179–194 (2014).
64. B. Efron, R. Tibshirani, *An Introduction to the Bootstrap*, (Chapman & Hall, New York, 1994).

Downloaded at Palestinian Territory, occupied on December 11, 2021

www.manaraa.com